




# XMM-Newton and NICER Measurement of the Rms Spectrum of the Millihertz Quasiperiodic Oscillations in the Neutron-star Low-mass X-Ray Binary 4U 1636–53

Ming Lyu<sup>1,2</sup>, Guobao Zhang<sup>3,4</sup> , Mariano Méndez<sup>5</sup>, D. Altamirano<sup>6</sup>, G. C. Mancuso<sup>7,8</sup>, Fu-Yuan Xiang<sup>1,2</sup>, and Huaping Xiao<sup>1,2</sup>

<sup>1</sup> Department of Physics, Xiangtan University, Xiangtan, Hunan 411105, People's Republic of China; [lvming@xtu.edu.cn](mailto:lvming@xtu.edu.cn)

<sup>2</sup> Key Laboratory of Stars and Interstellar Medium, Xiangtan University, Xiangtan, Hunan 411105, People's Republic of China

<sup>3</sup> Yunnan Observatories, Chinese Academy of Sciences (CAS), Kunming 650216, People's Republic of China

<sup>4</sup> Key Laboratory for the Structure and Evolution of Celestial Objects, CAS, Kunming 650216, People's Republic of China

<sup>5</sup> Kapteyn Astronomical Institute, University of Groningen, P.O. Box 800, NL-9700 AV Groningen, The Netherlands

<sup>6</sup> Physics & Astronomy, University of Southampton, Southampton, Hampshire SO17 1BJ, UK

<sup>7</sup> Instituto Argentino de Radioastronomía (CCT-La Plata, CONICET; CICPBA), C.C. No. 5, 1894 Villa Elisa, Argentina

<sup>8</sup> Facultad de Ciencias Astronómicas y Geofísicas, Universidad Nacional de La Plata, Paseo del Bosque s/n, 1900 La Plata, Argentina

Received 2019 November 19; revised 2020 April 20; accepted 2020 April 21; published 2020 June 3

## Abstract

We used two XMM-Newton and six Neutron Star Interior Composition Explorer observations to investigate the fractional rms amplitude of the millihertz quasiperiodic oscillations (mHz QPOs) in the neutron-star low-mass X-ray binary 4U 1636–53. We studied, for the first time, the fractional rms amplitude of the mHz QPOs versus energy in 4U 1636–53 down to 0.2 keV. We find that, as the energy increases from  $\sim 0.2$  to  $\sim 3$  keV, the rms amplitude of the mHz QPOs increases, different from the decreasing trend that has been previously observed above 3 keV. This finding has not yet been predicted by any current theoretical model; however, it provides an important observational feature to speculate whether a newly discovered mHz oscillation originates from the marginally stable nuclear burning process on the neutron-star surface.

*Unified Astronomy Thesaurus concepts:* Low-mass x-ray binary stars (939); Neutron stars (1108); Astrophysical explosive burning (100)

## 1. Introduction

A distinct class of quasiperiodic oscillations (QPOs) was discovered by Revnivtsev et al. (2001) in the neutron-star low-mass X-ray binaries (LMXBs) 4U 1636–53, 4U 1608–52, and Aql X–1. The typical frequency of these QPOs is  $\sim 5$ –14 mHz (Revnivtsev et al. 2001; Altamirano et al. 2008; Lyu et al. 2015; Strohmayer et al. 2018; Mancuso et al. 2019), and the QPOs become undetectable once there is an onset of a type I X-ray burst (Revnivtsev et al. 2001; Altamirano et al. 2008). The millihertz (mHz) QPOs are present only when the source luminosity is within a narrow range,  $L_{2-20 \text{ keV}} \simeq (5-11) \times 10^{36} \text{ erg s}^{-1}$  (Revnivtsev et al. 2001; Altamirano et al. 2008), and are more significant at low energies ( $< 5$  keV). Revnivtsev et al. (2001) proposed that the mHz QPOs originate from a special mode of nuclear burning on the neutron-star surface. This interpretation was consistent with the finding that in 4U 1608–52 the 2–5 keV count rate connected with a 7.5 mHz QPO is anticorrelated with the frequency of the kilohertz (kHz) QPOs (Yu & van der Klis 2002): the inner disk is “pushed” outwards by the radiation stresses from the neutron-star surface in each mHz QPO cycle when the luminosity increases, leading to the change of the kHz QPO frequency. In the work of Altamirano et al. (2008), it is found that the mHz QPOs in 4U 1636–53 show a systematically decreasing frequency before a type I X-ray burst when the source was in the transitional state. A similar behavior was also reported in the LMXB EXO 0748–676 by Mancuso et al. (2019). These frequency drifts indicate that there is a close connection between the QPOs and the nuclear burning on the neutron-star surface.

Calculations in Heger et al. (2007) suggest that the mHz QPOs originate from marginally stable nuclear burning of helium on the neutron-star surface. Their simulation shows an oscillatory mode of burning at a characteristic timescale of  $\sim 100$  s, consistent with the  $\sim 2$  minute period of the mHz QPOs (Heger et al. 2007). The

burning is oscillatory only when the accretion rate close to the Eddington rate, one order of magnitude bigger than the global accretion rate implied from observations. Keek et al. (2009) found that the turbulent chemical mixing of the fuel, together with a higher heat flux from the crust, is able to generate the mHz QPOs at the observed accretion rate. In their simulation, the frequency drift of the QPOs could be triggered if there is a cooling process of the burning layer. Keek et al. (2014) further studied the influence of the nuclear reaction rate and the fuel composition in producing the mHz QPOs. They found that, at the observed accretion rate, the mHz QPOs could not be triggered by changing only the composition and the reaction rate.

Millihertz QPOs with different observational properties were reported by Linares et al. (2010) in the neutron-star transient source IGR J17480–2446. These so-called “high-luminosity” mHz QPOs have a frequency of  $\sim 4.5$  mHz, and the persistent luminosity of the source when the mHz QPOs were present was relatively high,  $L_{2-50 \text{ keV}} \sim 10^{38} \text{ erg s}^{-1}$ . Interestingly, as the accretion rate increased, type I X-ray bursts in IGR J17480–2446 gradually evolved into a mHz QPO, and vice versa (Linares et al. 2012).

More recently, Stiele et al. (2016) found that the oscillations in 4U 1636–53 were not consistent with the variations of the temperature of the neutron-star surface, whereas Strohmayer et al. (2018) found that the oscillations in GS 1826–238 were due to the blackbody temperature modulation, assuming a constant blackbody normalization in the oscillation cycles. Lyu et al. (2015) found that, in 4U 1636–53, the frequency of the mHz QPOs is not significantly correlated with the temperature of the neutron-star surface, different from theoretical predictions (Heger et al. 2007; Keek et al. 2009). Lyu et al. (2016) showed that the 39 type I X-ray bursts associated with mHz QPOs in 4U 1636–53 all show positive convexities (Maurer & Watts 2008) and short rising time (Mahmoodifar & Strohmayer 2016), indicating that the mHz

QPOs in this source originate at the equatorial region of the neutron-star surface. The finding of Lyu et al. (2016) also suggests that the local mass accretion rate, from an equatorial accretion disk, could be higher than the global averaged accretion rate, possibly offering a solution to the apparent discrepancy between the model predictions and the observations. Lyu et al. (2019a) investigated the mHz QPOs in 4U 1636–53 using all available Rossi X-ray Timing Explorer (RXTE) observations and found that there was no mHz QPO when the source was in the hard state. Furthermore, Lyu et al. (2019a) found that the absolute rms amplitude of the mHz QPOs was independent of the parameter  $S_a$ , which is assumed to be an increasing function of the accretion rate (Hasinger & van der Klis 1989; Méndez et al. 1999; Zhang et al. 2011).

In this paper we studied, for the first time, the amplitude of the mHz QPOs versus energy in 4U 1636–53 down to 0.2 keV with XMM-Newton and Neutron Star Interior Composition Explorer (NICER) observations. The paper is organized as follows: we describe the observations and the details of the data reduction and analysis in Section 2. In Section 3 we show results derived in this work. In Section 4, we discuss the findings in the frame of a marginally stable nuclear burning process.

## 2. Observations and Data Reduction

In this work we used data taken from XMM-Newton and NICER. The XMM-Newton observations were performed on 2008 February 27 (ObsID: 0500350401, label “X1”) and 2009 March 14 (ObsID: 0606070101, label “X2”) using the European Photon Imaging Camera, EPIC-PN (Strüder et al. 2001), in timing mode. Millihertz QPOs have already been reported in these two observations in previous works (Lyu et al. 2015; Stiele et al. 2016).

We used the Science Analysis System (SAS) version 16.1.0 for the XMM-Newton data reduction, with the latest calibration files applied. We extracted calibrated events with the tool `epproc`, and applied the command `barycen` to convert the arrival time of photons from the local satellite frame to the barycenter of the solar system. We further applied the SAS task `epiclccorr` to correct the EPIC source time series. We applied the test `epatplot` and found that there was moderate pileup in the X1 and X2. We then selected a 41-column-wide region centered at the position of the source, and excluded the central three and one columns for the X1 and X2 observations, respectively. We selected only single and double events (`pattern ≤ 4`) to extract 1 s light curves.

We excluded instrument dropouts and X-ray bursts, and produced a light curve from 0.5 to 5.3 keV for each XMM-Newton observation. We made dynamic power spectra of these two XMM-Newton observations (Figure 1) to locate the time interval during which the mHz QPOs were present. The mHz QPOs are not always present in these two observations and the frequency of the QPO shows clear changes with time. We selected the data set D1, time interval 24,860–33,052 s from the start of the observation in X1, and D2, time interval 0–16,384 s from the start of the observation in X2, where the variation of the QPO frequency is less than 1 mHz (see Table 1 and Figure 1 for more details). We then divided the data sets D1 and D2 into several 2048 s segments (s1–s4 in X1, s1–s8 in X2; see Table 1 for more information), and extracted light curves in different energy bands (0.5–1.3; 1.3–2.1; 2.1–2.9; 2.9–3.7; 3.7–4.5; 4.5–5.3 keV) for all the segments.

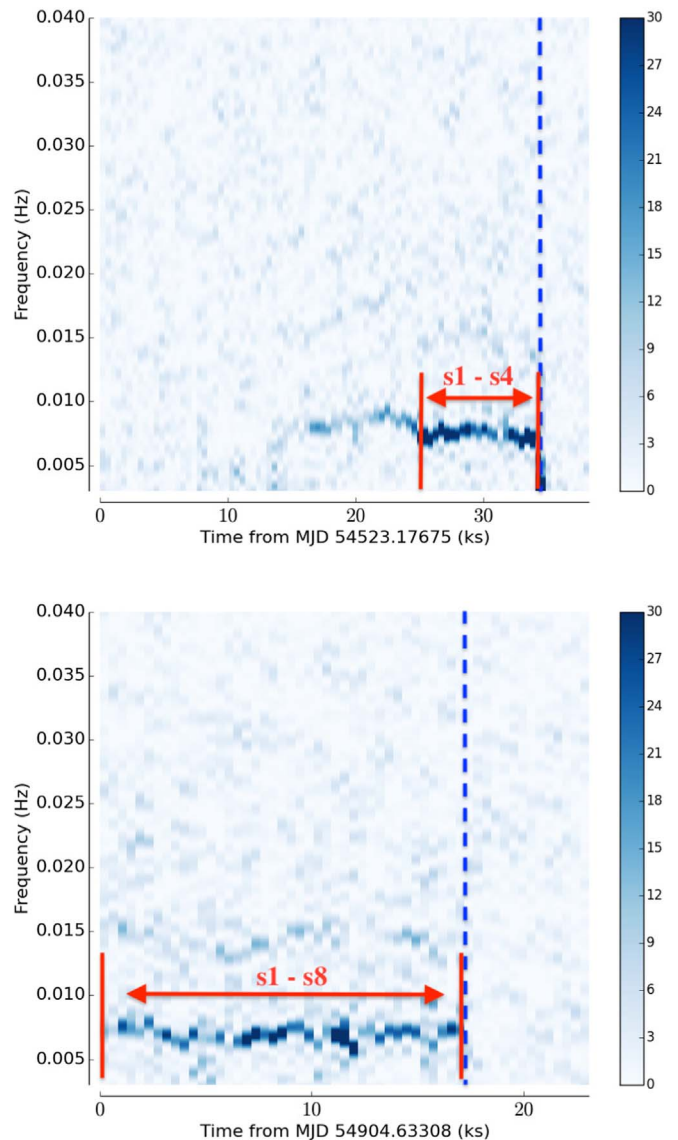


**Figure 1.** Dynamic power spectra of the two XMM-Newton observations (top: 0500350401; bottom: 0606070101) of 4U 1636–53. Each column represents the power spectrum generated from an 840 s time interval with the starting time of each interval set to 420 s after the starting time of the previous one. To display the frequency evolution, the frequency is oversampled by a factor of 100 using the Lomb–Scargle periodogram. We fixed the count rate within instrument dropouts and X-ray bursts at the average rate of the whole observation. The color bars on the right indicate the power at each frequency. We marked the range of the data sets D1 (s1–s4) and D2 (s1–s8) used in this work. The blue dashed line indicates the time of the onset of a type I X-ray burst in each observation.

We analyzed all 124 NICER observations of 4U 1636–53 available in the archive at the time we wrote this paper. The NICER data were processed following standard procedures using the NICER Data Analysis Software NICERDAS 2018 October 7 V005, together with HEASOFT version 6.25. We cleaned the data using standard calibration process with `nicercal` and applied standard screening with `nimake-time` in the full level 2 calibration and screening pipeline `nicerl2`. We then extracted a light curve in the 0.2–5.0 keV range at a 1 s resolution for each NICER observation using `xselect` and searched them for mHz oscillations using Lomb–Scargle periodograms (Lomb 1976; Scargle 1982). Among all NICER observations, six of them show significant

**Table 1**  
XMM-Newton and NICER Observations of the mHz QPOs in 4U 1636–53

Observation ID	Segment	Time Range (s)	Average Frequency (mHz)	Rms Amplitude (%)
0500350401 (X1)	s1	24860–26908	$7.22 \pm 0.03$	$1.32 \pm 0.14$
	s2	26908–28956	$7.49 \pm 0.04$	$0.98 \pm 0.14$
	s3	28956–31004	$7.63 \pm 0.04$	$0.99 \pm 0.14$
	s4	31004–33052	$7.27 \pm 0.04$	$0.85 \pm 0.14$
0606070101 (X2)	s1	0–2048	$7.35 \pm 0.03$	$0.85 \pm 0.11$
	s2	2048–4096	$7.13 \pm 0.04$	$0.69 \pm 0.11$
	s3	4096–6144	$6.66 \pm 0.03$	$0.88 \pm 0.11$
	s4	6144–8192	$6.77 \pm 0.03$	$1.00 \pm 0.11$
	s5	8192–10240	$7.43 \pm 0.03$	$0.92 \pm 0.11$
	s6	10240–12288	$6.80 \pm 0.03$	$1.05 \pm 0.11$
	s7	12288–14336	$7.08 \pm 0.03$	$0.94 \pm 0.11$
	s8	14336–16384	$7.43 \pm 0.04$	$0.78 \pm 0.11$
1050080128	...	11300–12950	$9.18 \pm 0.02$	$1.68 \pm 0.10$
1050080132	...	16700–18200	$8.71 \pm 0.03$	$1.61 \pm 0.11$
1050080144	...	0–480	$9.06 \pm 0.07$	$3.79 \pm 0.25$
1050080149	...	48490–49340	$7.80 \pm 0.08$	$1.10 \pm 0.13$
1050080151	...	38760–39570	$5.26 \pm 0.05$	$2.13 \pm 0.16$
1050080152	...	22460–22930	$11.16 \pm 0.10$	$2.60 \pm 0.22$

**Note.** All errors in the table are at the 68% confidence level. The rms amplitude is measured in the 0.5–5.3 keV and the 0.2–5.0 keV bands for the two XMM-Newton (X1, X2) and the NICER observations, respectively. In the two XMM-Newton observations, the errors of the rms amplitude in different segments in the same observation are the same after being rounded off at two decimals.

mHz QPOs (see, e.g., Figure 2). The significance, as estimated from the Lomb–Scargle periodogram, are in all cases above the  $3\sigma$  confidence level, taking into account the number of trials. For these six observations, we then extracted light curves in different energy bands (0.2–1.0; 1.0–1.8; 1.8–2.6; 2.6–3.4; 3.4–4.2; 4.2–5.0 keV).

As with each XMM-Newton observation, we fitted the 0.5–5.3 keV light curve with mHz QPOs with a model consisting of a sine function plus a constant to get general properties of the QPOs. We then used the best-fit period to fold the light curves in different energy bands using the `ftool` `efold`. For the NICER observations, we applied the same procedure to fit the 0.2–5.0 keV light curves and folded light curves in different energy bands.

Besides, we made a soft-color–intensity diagram (SID) to trace the spectral state of the source in these six NICER observations. The soft color was computed as the ratio of count rates in the 1.8–3.5 and 0.5–1.8 keV bands using 32 s intervals, while the intensity was calculated as the rate in the 0.5–6.8 keV band (Bult et al. 2018).

We then evaluated the influence of the background in the calculation of fractional rms amplitude. For the XMM-Newton data in timing mode, the whole CCD was contaminated by the source photons due to the wide point-spread function of the telescope (Ng et al. 2010; Hiemstra et al. 2011; Sanna et al. 2013). To extract the background, we then selected the observation of 4U 1608–52 (ObsID 0074140201) in the same observational mode when the source was close to quiescence (Lyu et al. 2019b). The background is extracted from a region RAWX in [17:57] without including the time interval with a flaring particle. The derived ratio

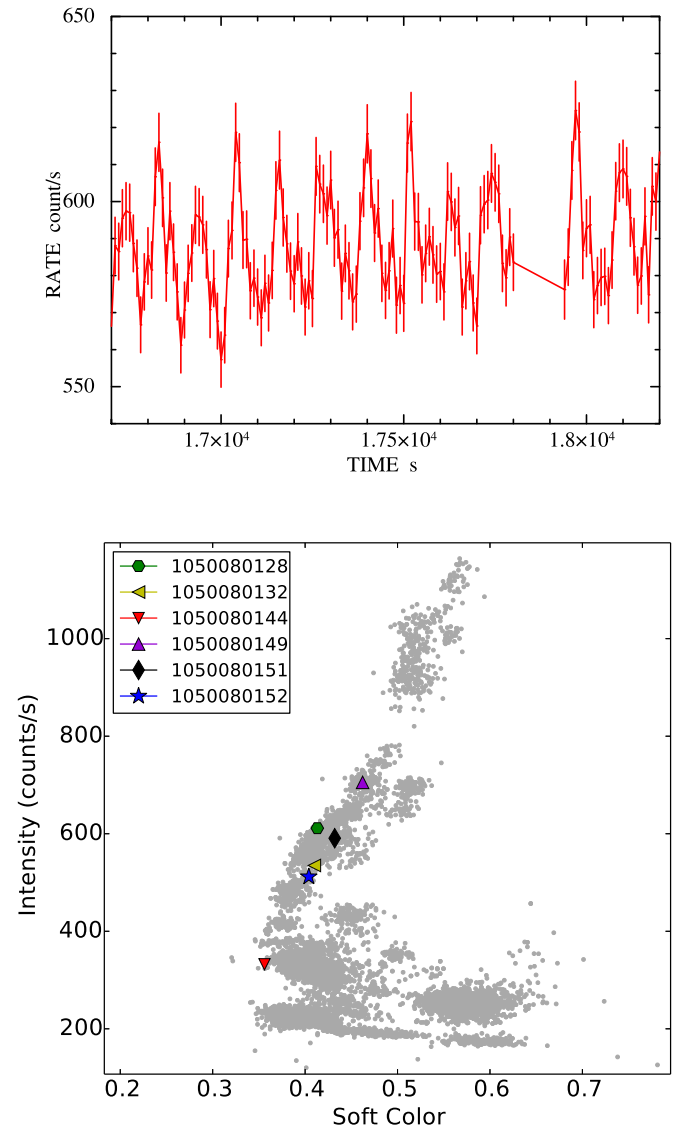


**Figure 2.** Light curve (ObsID:1050080132) and soft-color–intensity diagram (SID) of 4U 1636–53 with NICER. The light curve is in the 0.2–5.0 keV energy, with a time resolution of 10 s. Significant QPOs are present at a timescale of  $\sim 110$  s. The soft color in the SID was computed as the ratio of count rates between the 1.8–3.5 keV and the 0.5–1.8 keV photons using 32 s intervals, while the intensity was calculated as the count rate in 0.5–6.8 keV.

of the background count rate to the total rate in each energy band is very small,  $\sim 0.2\%$ . On the other hand, the NICER background was estimated to be  $\sim 0.5$  counts  $s^{-1}$  keV $^{-1}$  at  $\sim 0.6$  keV and  $\sim 0.1$  counts  $s^{-1}$  keV $^{-1}$  above  $\sim 1.4$  keV (Keek et al. 2018). Therefore, in the following analysis we do not take the background into account in the calculations since it is smaller than the errors of the fractional rms amplitude.

Finally, we fitted each folded light curve with a function consisting of a constant term plus a sine function with the period fixed at 1, and calculated the fractional rms amplitude of the mHz QPO in different bands,  $rms = A/[\sqrt{2} * C]$ , where  $A$  is the amplitude of the sine function and  $C$  is the value of the constant component. For the two XMM-Newton observations, the final rms amplitude is then derived as the average of the rms amplitudes in all time segments. For the NICER observations, we calculated the rms amplitude directly in each observation since the time segments with mHz QPOs are very short, less than  $\sim 1500$  s.

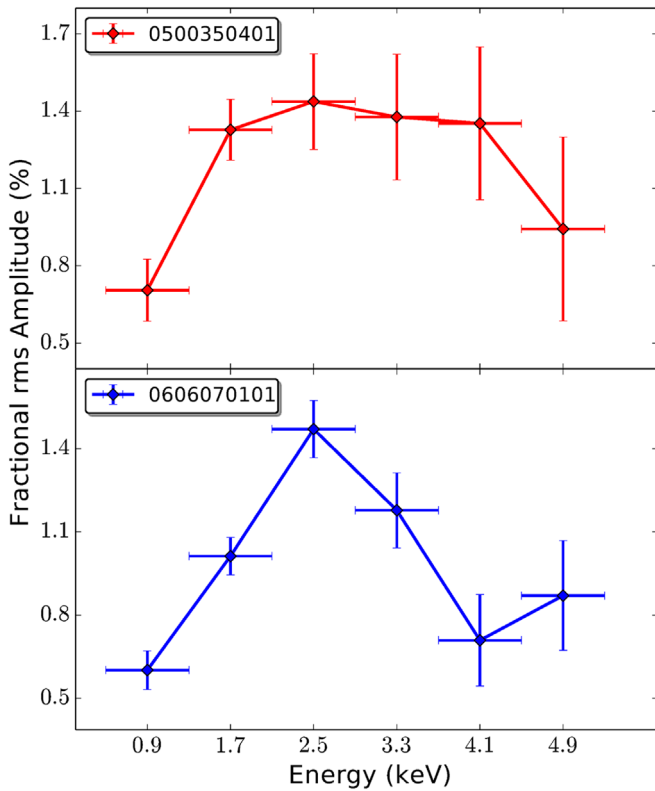


**Figure 3.** Fractional rms amplitude of the mHz QPOs in 4U 1636–53 as a function of energy for the two XMM-Newton observations (X1 to X2 from top to bottom). The energy in the plot represents the central energy of each band, with the error bar indicating the energy range of the band.

### 3. Results

In Table 1, we show the average frequency and the fractional rms amplitude of the mHz QPOs in the 0.5–5.3 keV and 0.2–5.0 keV energy bands for, respectively, the segments in the XMM-Newton and NICER observations. The average frequency of the mHz QPOs in the XMM-Newton observations was in the ranges 7.2–7.7 mHz and 6.6–7.5 mHz for the observations X1 and X2 in the 0.5–5.3 keV energy band, respectively. The fractional rms amplitude of the QPOs ranges from 0.85% to 1.32% in X1, and from 0.69% to 1.05% in X2. The mHz QPOs in the NICER observations cover a relatively wide frequency range, 5.2–11.1 mHz, with the rms amplitude in the 0.2–5.0 keV band being between 1.10% and 3.79%. In Figure 2, we show the distribution of the six NICER observations with mHz QPOs in the SID. Similar to the color diagram in Zhang et al. (2011) and Bult et al. (2018), the figure shows that the source went from the soft spectral state to the transitional spectral state as it moved from the top to the bottom left in the diagram, and then the source moved to the hard spectral state when it went to the bottom right. The intensity and the soft color for these six NICER observations are in the ranges 300–800 and 0.35–0.5 counts  $s^{-1}$ , respectively, when the source was in the intermediate/transitional spectral state (see, e.g., Bult et al. 2018).

In Figure 3, we show the fractional rms amplitude of the mHz QPOs versus energy in the two XMM-Newton observations. The rms amplitude first increases from  $\sim 0.6\%$  at 0.9 keV to  $\sim 1.4\%$  at 2.5 keV, and then decreases as the energy further increases. The mHz QPOs in the NICER observations follow a similar trend,

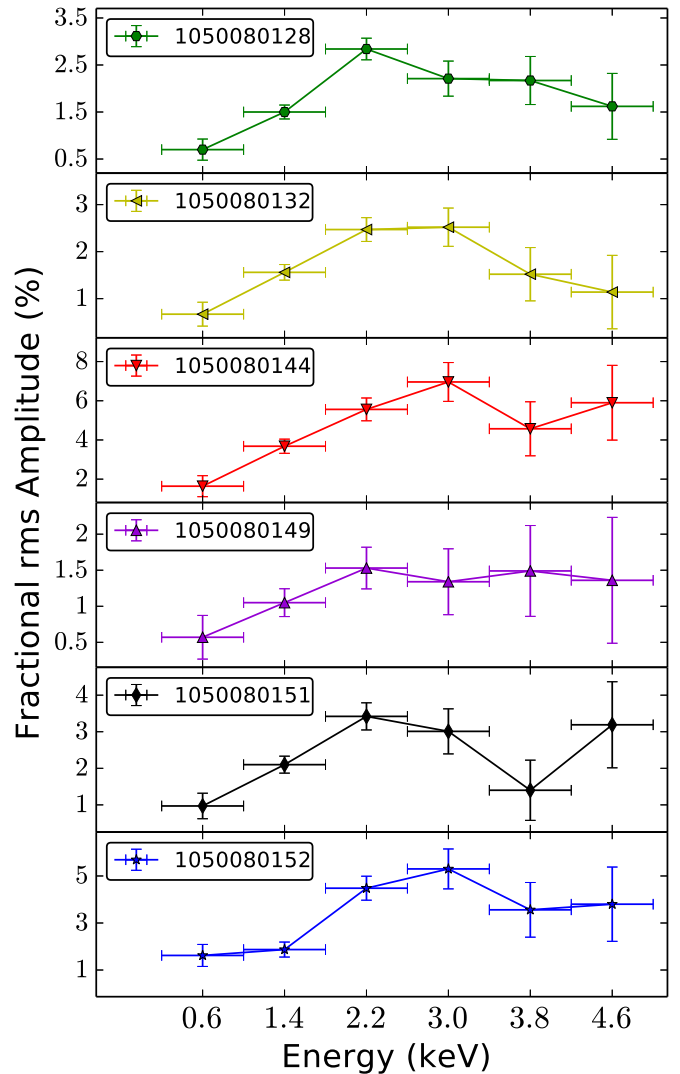


**Figure 4.** Fractional rms amplitude of the mHz QPOs in 4U 1636–53 as a function of energy for the NICER observations. The energy in the plot represents the central energy of each band, with the error bar indicating the energy range of the band.

although errors of the fractional rms amplitude at energies  $> 3$  keV in some observations are relatively large. As shown in Figure 4, the rms amplitude of the QPO in each NICER observation generally increases from 0.2 to 2.2–3.0 keV, and then decreases or remains more or less constant as the energy further increases up to 5.0 keV.

### 4. Discussion

We studied the fractional rms amplitude of the mHz QPOs versus energy in 4U 1636–53 with XMM-Newton and NICER. For the first time, we found that the fractional rms amplitude of the mHz QPOs in 4U 1636–53 increases from 0.2 to 2.5–3.0 keV, different from the trend observed above 3 keV with RXTE (Revnivtsev et al. 2001; Altamirano et al. 2008).

With NICER observations, Strohmayer et al. (2018) found that in GS 1826–238 there is a clear increasing trend of the rms amplitude of the mHz QPOs from 1 to 3 keV. Our results on the XMM-Newton and the NICER observations of 4U 1636–53 show a clear increasing trend up to  $\sim 3$  keV, indicating that the mHz QPOs in 4U 1636–53 have the same trend as in GS 1826–238

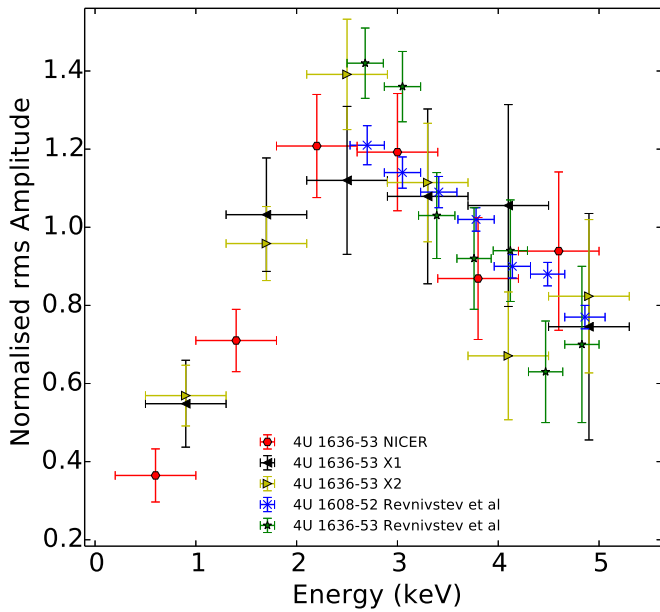


**Figure 5.** Normalized rms amplitude of the mHz QPOs as a function of energy for the XMM-Newton and the NICER observations in this work plus the RXTE observations in Revnivtsev et al. (2001). We rescaled all the rms spectra of the mHz QPOs in the NICER observations by their average and calculated the mean of the rescaled rms at each energy. We then normalized all the rms spectra in this work and in Revnivtsev et al. (2001) by their averages in the 2.5–5 keV range to bring them to the same scale for comparison. The energy in the plot represents the central energy of each band, with the error bar indicating the energy range of the band.

below 3 keV. Considering that the mHz QPOs in both 4U 1636–53 and GS 1826–238 show an increasing trend as energy increases up to 3 keV, it is likely that this is an intrinsic feature of this type of QPO.

The rms amplitude derived in the XMM-Newton observations decreases as the energy further increases above 3 keV, consistent with the previous results with RXTE observations. Using RXTE data, Revnivtsev et al. (2001) found that in 4U 1608–52 and 4U 1636–53 the fractional rms amplitude decreases with energy from 2.5 to 5 keV. In the NICER observations the rms amplitude above 3 keV is consistent with either decreasing or remaining more or less constant. We further divided the rms spectrum of the mHz QPO in each NICER observation by its average for comparison. We found that the rescaled rms spectra in all NICER observations were consistent with being the same within errors. We then calculated the average of these rescaled rms at each energy. Finally, we rescaled the averaged NICER rms spectrum, the XMM-Newton rms spectra, and the rms spectra in Revnivtsev et al. (2001) by their averages in the 2.5–5 keV range to bring them to the same scale for comparison. As shown in Figure 5, the normalized rms spectra above  $\sim 2.5$  keV in this work are consistent with the ones in Revnivtsev et al. (2001). These normalized rms spectra further confirm that the fractional rms amplitude of the mHz QPOs first increases and then decreases as the energy increases, with the turnover point around 2.5–3.0 keV.

Thanks to the low-energy coverage provided by NICER and XMM-Newton, we were able to show, for the first time, that there is a change in the rms amplitude versus energy relation of the mHz QPOs in 4U 1636–53 around 2.5–3.0 keV. The mechanism responsible for this change is still an open question. Existing models connect the rms amplitude variation to the change of the accretion rate and the crust luminosity; however, to our knowledge

neither of them could potentially explain the change of the rms spectra found in this work. In the model of Heger et al. (2007), as the accretion rate varies, the transition between stable and unstable burning naturally leads to significant changes in the amplitude of the mHz QPOs. Notwithstanding, the work of Lyu et al. (2019a) indicates that in 4U 1636–53 there is no significant correlation between the absolute rms amplitude and the parameter  $S_{\text{crust}}$ , which is assumed to be an increasing function of the accretion rate (Hasinger & van der Klis 1989; Méndez et al. 1999; Zhang et al. 2011).

Keek et al. (2009) found that in their model the simulated mHz QPOs exhibit an increasing amplitude when the heat flux from the neutron-star crust decreases, and that the amplitude of oscillatory burning becomes much larger when considering the turbulent chemical mixing of the fuel. Apparently, the energy dependence of the rms amplitude of the mHz QPOs could not be interpreted in this scenario. More work is still needed to understand the mechanism behind this relation. Interestingly, type I X-ray bursts in this source have a color temperature around 2 keV (Zhang et al. 2011), which is close to the turnover point of the derived rms amplitude versus energy relation derived in this work. Both the mHz QPOs and type I X-ray bursts originate from nuclear burning on the neutron-star surface (e.g., Paczynski 1983; Cumming 2004; Heger et al. 2007; Keek et al. 2009), and the model of the mHz QPOs also predicts the evolution between the mHz QPOs and bursts seen in observations (see Figure 5 in Heger et al. 2007 and Figure 9 in Keek et al. 2009 for more details). It is possible that both the color temperature of the bursts and the turnover point of the rms amplitude versus energy relation are connected to the same physical factor on the neutron-star surface.

Ferrigno et al. (2017) reported a strong QPO at  $\sim 8$  mHz in the accreting millisecond X-ray pulsar IGR J00291+5934 in an XMM-Newton observation. The frequency of this 8 mHz QPO did not drift, and the QPO was present throughout the entire observation. Ferrigno et al. (2017) found that the rms amplitude of the QPO was around 29% at  $\sim 0.7$  keV and decreased dramatically as the energy increased, reaching  $\sim 7\%$  at around 6–10 keV. The physical origin of this 8 mHz QPO is still uncertain. The possibility that this 8 mHz QPO is connected to marginally stable nuclear burning on the neutron-star surface can neither be excluded nor more solidly confirmed. The reason is that there has been only one type I X-ray burst ever detected in this source, which occurred about three days before this XMM-Newton observation (de Falco et al. 2017). The rms amplitude versus energy relation derived in this work and the work of Strohmayer et al. (2018) may help us decide whether this 8 mHz QPO originates from nuclear burning. The rms amplitude of the mHz QPOs in both 4U 1636–53 and GS 1826–238 increases with energy below 3 keV. Considering that, compared to the mHz QPOs in these two sources, the 8 mHz QPO in IGR J00291+5934 shows a decreasing rms amplitude as energy increases below 3 keV, together with the fact that the rms amplitude in IGR J00291+5934 is at least an order of magnitude larger than the ones in other mHz QPOs, suggests that the 8 mHz QPO in IGR J00291+5934 does not originate from marginally stable nuclear burning on the neutron-star surface.

This work is based on observations obtained with XMM-Newton, an ESA science mission with instruments and contributions directly funded by ESA Member States and NASA. This research has made use of data obtained from the

High Energy Astrophysics Science Archive Research Center (HEASARC), provided by NASA Goddard Space Flight Center. This research made use of NASA's Astrophysics Data System. Lyu is supported by National Natural Science Foundation of China (grant No. 11803025) and the Hunan Provincial Natural Science Foundation (grant No. 2018JJ3483). G.B. acknowledges funding support from the National Natural Science Foundation of China (NSFC) under grant No. U1838116 and the CAS Pioneer Hundred Talent Program Y7CZ181002. D.A. acknowledges support from the Royal Society. G.C.M. and D.A. acknowledge support from the Royal Society International Exchanges "The first step for High-Energy Astrophysics relations between Argentina and UK." G.C.M. was partially supported by PIP 0102 (CONICET) and received financial support from PICT-2017-2865 (ANPCyT). F.Y.X. is supported by the Joint Research Funds in Astronomy (U1531108 and U1731106). H.P.X. is supported by National Natural Science Foundation of China (grant No. 11473023).

*Facilities:* XMM-Newton, NICER.

*Software:* SAS 16.1.0, HEASOFT 6.25, NICERDAS 2018 October 7, Python 3.6.5.

### ORCID iDs

Guobao Zhang  <https://orcid.org/0000-0001-8630-5435>

### References

- Altamirano, D., van der Klis, M., Wijnands, R., & Cumming, A. 2008, *ApJL*, **673**, L35  
 Bult, P., Altamirano, D., Arzoumanian, Z., et al. 2018, *ApJL*, **860**, L9

- Cumming, A. 2004, *NuPhS*, **132**, 435  
 de Falco, V., Kuiper, L., Bozzo, E., et al. 2017, *A&A*, **599**, A88  
 Ferrigno, C., Bozzo, E., Sanna, A., et al. 2017, *MNRAS*, **466**, 3450  
 Hasinger, G., & van der Klis, M. 1989, *A&A*, **225**, 79  
 Heger, A., Cumming, A., & Woosley, S. E. 2007, *ApJ*, **665**, 1311  
 Hiemstra, B., Méndez, M., Done, C., et al. 2011, *MNRAS*, **411**, 137  
 Keek, L., Arzoumanian, Z., Bult, P., et al. 2018, *ApJL*, **855**, L4  
 Keek, L., Cyburt, R. H., & Heger, A. 2014, *ApJ*, **787**, 101  
 Keek, L., Langer, N., & in't Zand, J. J. M. 2009, *A&A*, **502**, 871  
 Linares, M., Altamirano, D., Chakrabarty, D., Cumming, A., & Keek, L. 2012, *ApJ*, **748**, 82  
 Linares, M., Altamirano, D., Watts, A., et al. 2010, *ATel*, 2958, 1  
 Lomb, N. R. 1976, *Ap&SS*, **39**, 447  
 Lyu, M., Méndez, M., Altamirano, D., & Zhang, G. 2016, *MNRAS*, **463**, 2358  
 Lyu, M., Méndez, M., Altamirano, D., Zhang, G., & Mancuso, G. C. 2019a, *ApJ*, **885**, 5  
 Lyu, M., Méndez, M., Zhang, G., & Keek, L. 2015, *MNRAS*, **454**, 541  
 Lyu, M., Méndez, M., Zhang, J.-F., & Xiang, F.-Y. 2019b, *MNRAS*, **484**, 3434  
 Mahmoodifar, S., & Strohmayer, T. 2016, *ApJ*, **818**, 93  
 Mancuso, G. C., Altamirano, D., García, F., et al. 2019, *MNRAS: Lett.*, **486**, L74  
 Maurer, I., & Watts, A. L. 2008, *MNRAS*, **383**, 387  
 Méndez, M., van der Klis, M., Ford, E. C., Wijnands, R., & van Paradijs, J. 1999, *ApJL*, **511**, L49  
 Ng, C., Díaz Trigo, M., Cadolle Bel, M., & Migliari, S. 2010, *A&A*, **522**, A96  
 Paczynski, B. 1983, *ApJ*, **264**, 282  
 Revnivtsev, M., Churazov, E., Gilfanov, M., & Sunyaev, R. 2001, *A&A*, **372**, 138  
 Sanna, A., Hiemstra, B., Méndez, M., et al. 2013, *MNRAS*, **432**, 1144  
 Scargle, J. D. 1982, *ApJ*, **263**, 835  
 Stiele, H., Yu, W., & Kong, A. K. H. 2016, *ApJ*, **831**, 34  
 Strohmayer, T. E., Gendreau, K. C., Altamirano, D., et al. 2018, *ApJ*, **865**, 63  
 Strüder, L., Briel, U., Dennerl, K., et al. 2001, *A&A*, **365**, L18  
 Yu, W., & van der Klis, M. 2002, *ApJL*, **567**, L67  
 Zhang, G., Méndez, M., & Altamirano, D. 2011, *MNRAS*, **413**, 1913